JOURNAL OF MATERIALS SCIENCE 33 (1998) 271–278

Study of electrical characteristics and microstructure of zinc oxide varistor through rate-controlled sintering

D. HUDA*, M. A. EL BARADIE, M. S. J. HASHMI
School of Mechanical and Manufacturing Engineering, Dublin City University, Dublin 9, Ireland

R. PUYANE
Harris Ireland, The Demesne, Dundalk, Ireland

A computer program has been developed to control the firing process of ZnO varistors. The binder burnout and shrinkage stages are controlled through a closed feedback loop using a i286 based personal computer. The effect of rate-controlled sintering (RCS) on the formation of microstructure and simultaneously on electrical characteristics of varistors has been studied in arrester block with $V_{nom} = 5$ kV and a diameter of 42 mm. Leakage, watt loss and non-linear coefficient has been improved and microstructure with low porosity has been achieved by RCS.

1. Introduction

ZnO varistors are manufactured from doped ZnO ceramic powders. The doping powders are oxides of Bi, Sb, Co, Mn and Cr. A typical composition of varistor contains 97 mol % ZnO, 1 mol % Sb_2O_3 and 0.5 mol % of each of Bi_2O_3, CoO, MnO and Cr_2O_3 [1]. Varistors are formed by a sintering process. After sintering, the resultant product is a polycrystalline ceramic with a unique grain-boundary property that contributes to the well-known I–V characteristics of the device [2]. During this firing process, various chemical elements are distributed in such a way in the microstructure that the near-grain boundary region becomes highly resistive ($\rho_{gb} \approx 10^{12}\,\Omega$ cm) and the grain interior becomes highly conductive ($\rho_g \approx 1$ to $10\,\Omega$ cm).

The electrical characteristics of varistors are V_{nom}, IR value, clamp ratio and nature of I–V curve. Further details on the properties of zinc oxide varistors and their electrical characterization can be found in reference [3]. The I–V curve consists of three regions, pre-breakdown, break-down and upturn region. The low-current pre-breakdown linear region ($< 10^{-4}$ A cm^{-2}) has been identified to be controlled by the grain-boundary resistance and capacitance; and on the other end of the I–V curve, the high current linear region ($> 10^{3}$ A cm^{-2}) has been identified to be controlled by the impedance of the grain. The intermediate non-linear region, the region of major importance for a variety of applications is indirectly controlled by the resistivity differential between the grain boundary and the grain [2].

The secondary phase materials which are formed during firing are spinel [$Zn_7Sb_2O_{12}$], and Bi_2O_3 rich phases (consists of an amorphous phase αBi_2O_3 and pyrochlore [$Zn_2Bi_3Sb_3O_{14}$]) [4]. The main constituent of microstructure is ZnO grain ($\sim 15\,\mu$m grain size for arrester block applications) which are interspersed with smaller grains (~ 2 to $4\,\mu$m grain size). Spinel grains are usually located in clusters and surrounded by Bi-rich phases. Spinel grains contain dissolved chromium, manganese, cobalt and nickel. Bi-rich phases were visible at many grain boundaries and within clusters of śpinel grains [5]. The electrical characteristics improved if the varistors has a microstructure with smaller grain size. αBi_2O_3 and pyrochlore crystallized during cooling after sintering [5]. Bi_2O_3 is molten above 825 °C, assisting in initial densification of the polycrystalline ceramic. Bi_2O_3 increases grain size and density up to 1100 °C, whereas the density decreases with Bi_2O_3 content beyond this temperature [6]. This could be due to the significant evaporation of Bi_2O_3 at higher temperature in view of its higher vapour pressure. Sb_2O_3 inhibits the grain growth and simultaneously reduces density. This effect can be attributed to the formation of spinel phase which becomes anchored within the ZnO grains, thereby impeding material transport [6]. A small addition of Cr_2O_3 and NiO to ZnO in the presence of other additive oxides increase the breakdown voltage by

*Present address: Department of Mechanical and Manufacturing Engineering, Faculty of Engineering, Universiti Putra Malaysia, 43400, Serdang, Selangor, Malaysia.

0022–2461

TABLE I Ceramic powder characteristics

Powder	Average particle size (μm)	Density		Binder content ($g\,kg^{-1}$)	Moisture content (g/kg^{-1})	Binder type
		Bulk $g\,cm^{-3}$	Tap $g\,cm^{-3}$			
Standard	15–20	1.785	2.02	15	0.90	B

decreasing the grain size of the composite and addition of Al_2O_3 decreases the pore volume of the varistor [7] which is an important parameter to be considered for the improvement of energy handling capability. The breakdown characteristic is that it is relatively insensitive to the details of chemical composition and processing within reasonable limits [8]. The breakdown voltage ($E_{0.5}$ at $0.5\,mA\,cm^{-2}$) is decreased with increased sintering temperature and soaking time and the I–V curves are depressed. These results are due to the increasing grain size (fewer grain boundaries) of the ceramic as a result of increasing sintering temperature and time [9]. A small value of leakage current is preferable to varistor application. Acceptor doping reduces the leakage current whereas donor doping increases the leakage current [10–12]. Monovalent Li^+, an acceptor in ZnO, pushes the I–V curve to the left of the undoped varistor and trivalent Al^{3+}, a donor in ZnO, pushes the I–V curve to the right of the undoped varistor [11].

Very little information is available in relation to the electrical and microstructure properties of varistors produced by rate-controlled sintering (RCS). In the present work, an attempt has been made to study the effect of RCS on microstructure and electrical characteristics with a view to understand the influence of RCS on the above properties. The studies on microstructure and electrical characteristics were therefore carried out for several RCS profiles and results are compared with those sintered by conventional profile.

2. Materials

Standard powders were used for the experiments. The general criteria of this powder are shown in Table I. Green discs were collected from the production line with 50% relative density.

3. Apparatus and Experimental Procedure

The experimental set-up for controlling the low temperature firing (i.e. binder burnout region) and high temperature firing (i.e. shrinkage) are shown in Figs 1 and 2, respectively. Both are feed-back loop control system. Fig. 1 shows that at a predetermined time, the weights of the samples are transmitted to the computer from balance, then binder burnout rate is calculated and the command is sent from the computer to the temperature controller to modify the heating rate of the furnace to maintain constant binder burnout rate. Similarly, at a predetermined time interval, the shrinkage data is transferred from the LVDT transducer through the signal conditioner to the computer and a command is sent to the temperature controller to change the heating rate for the furnace to maintain a constant shrinkage rate, which is illustrated in Fig. 2. The firing profiles which were generated for constant binder burnout and shrinkage rate,

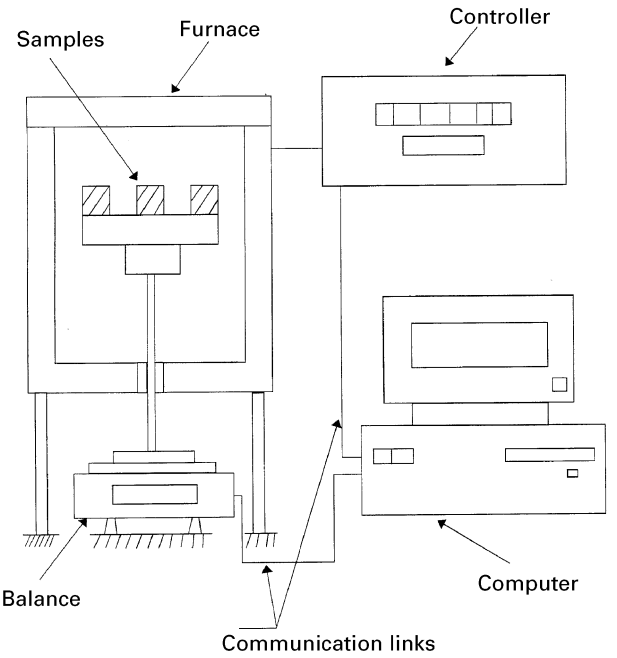

Figure 1 Sketch of the experimental set-up for binder burn-out control.

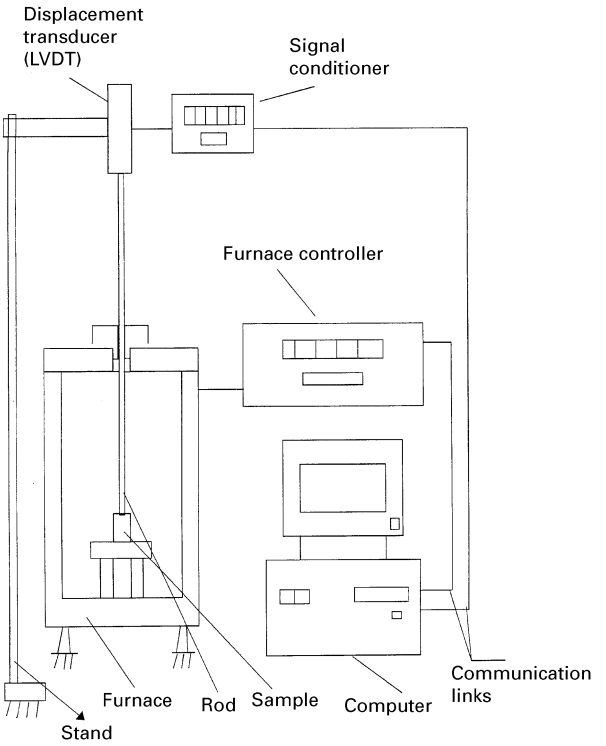

Figure 2 Sketch of the experimental set-up for shrinkage control.

TABLE II Firing profile numbers with weight loss rate and shrinkage rate and total firing time

Profile number	Weight loss rate ($g\,kg^{-1}\,h^{-1}$)	Shrinkage rate ($\mu m\,mm^{-1}h^{-1}$)	Total firing cycle time (h : min)
1	0.75	10	64 : 27
2	3	10	49 : 11
3	0.75	40	53 : 29
4	3	40	38 : 13
5	1.5	20	47 : 42
6 (classic profile)	Variable	Variable	69 : 15

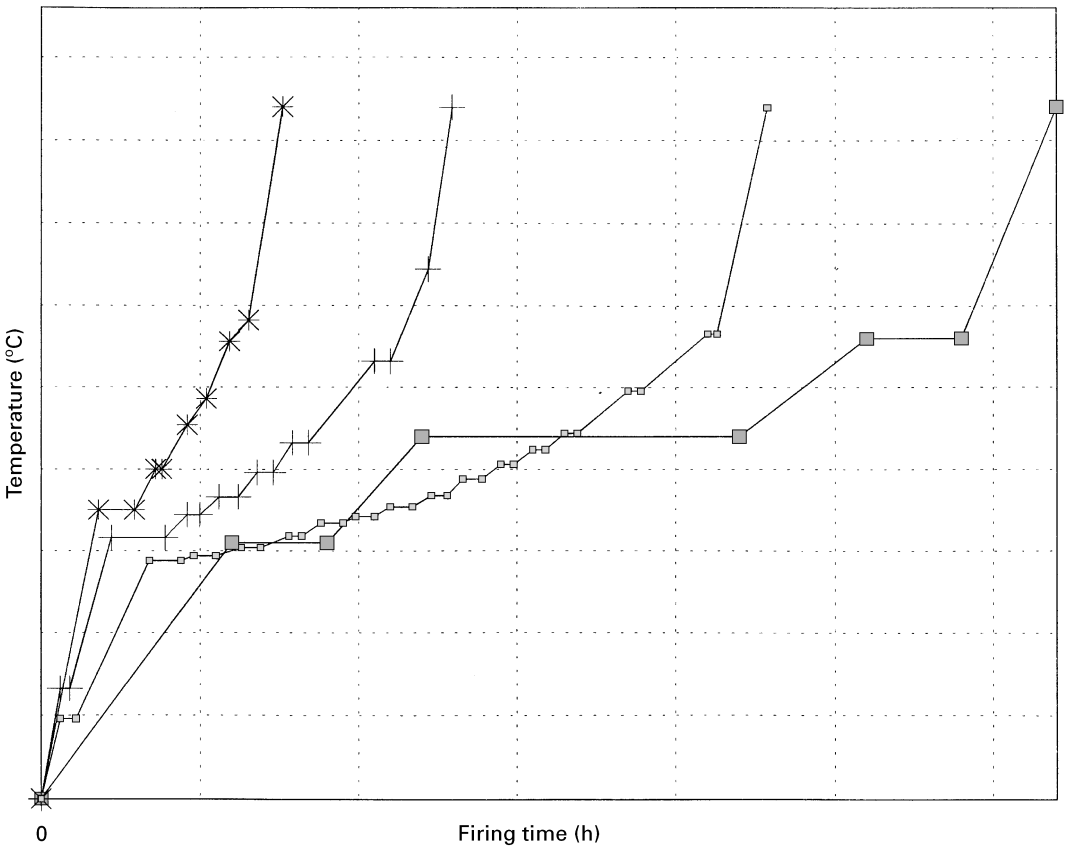

Figure 3 Temperature profiles for typical binder burn-out rates during RCS firing profile and classical profile (■) classical profile: RCS profile: (□) $0.75\,g\,kg^{-1}\,h^{-1}$; (+) $1.5\,g\,kg^{-1}\,h^{-1}$; (▩) $3\,g\,kg\,h^{-1}$.

were collected together to form the complete RCS profile. The peak temperature, time and cooling rate were used the same one as used in the conventional firing profile. Table II shows the profile number, weight loss rate, shrinkage rate and total firing cycle time of the above six firing profiles.

The sintering profile for the rate controlled sintering and conventional profile at the stages of binder burn-out (BBO) and shrinkage are shown in Figs 3 and 4, respectively. The complete sintering profile combines the profiles at BBO and shrinkage. It can be seen from these figures that for the RCS profiles, the binder burnout zone and the shrinkage zone have many ramps and dwell times and these are increased as the binder burn-out and shrinkage rates decrease. The Classic profile has small ramps and dwell time, but ramp rate is very low. The same cooling rate was maintained both for rate-controlled sintering and classical profile. Every time 10 discs were sintered in a pot kiln at the Development Facility at Harris Ireland using each one of the above sintering cycles. Fig. 5 shows the different steps for manufacturing ZnO varistors.

3.1. Grinding

After sintering, the black discs were ground at the top and bottom surfaces. The grinding was done using a diamond cutter with the accuracy of 0.00025 cm deviation of the cutting plane.

3.2. Ultrasonic Wash

After grinding, the samples were passed through an ultrasonic cleaner. The cleaning was carried out by cold water. The samples were placed on the rack of the rotating belt. First the samples were washed and then dried with a hot air jet.

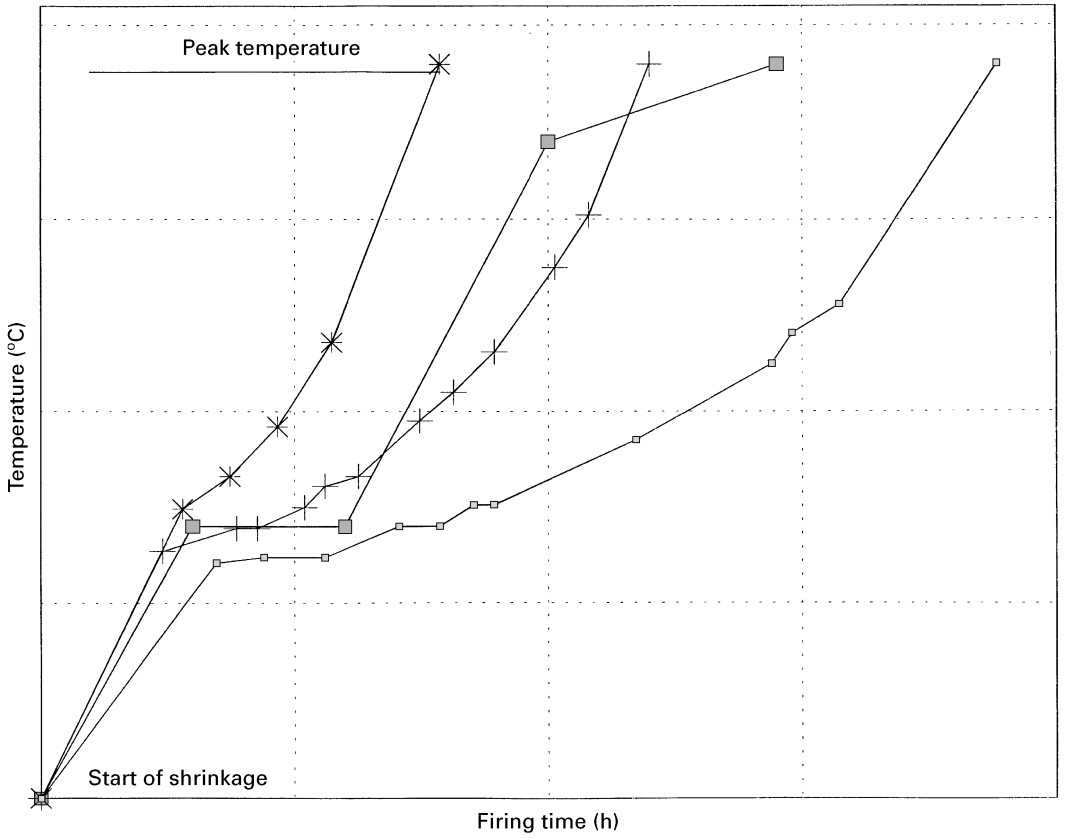

Figure 4 Temperature profiles at the shrinkage stage for RCS firing and classical firing (■): RCS firing; (∗) 40 μm mm^{-1} h^{-1}; (+) 20 μm mm^{-1} h^{-1}; (□) 10 μm mm^{-1} h^{-1}.

3.3. Electroding

Electroding was carried out by spraying molten aluminium particles on the top and bottom faces of the discs by an automatic arc spraying machine. Electroding is a crucial step for preparing the samples.

3.4. Buffing

The samples become rough after electroding, for proper working of the product, these surfaces should be cleaned. So after aluminium spraying, all the samples were cleaned by a grinding wheel which contains cotton wool on the grinding surface, by holding the sample against the wheel manually. This operation is called buffing.

3.5. Rewash

As during buffing the surfaces becomes full of dust, these are again washed by the ultrasonic bath and checked again whether the surfaces are properly electroded and cleaned. Normally all samples pass after rewash if electroding was done properly.

3.6. Glassing

The last stage for preparing the samples for electrical test is glassing. The side surface of the varistor block must be passivated to avoid flashover, i.e. the dielectric breakdown of the block surface–air interface. Passivation is achieved by coating the blocks with a glass coating. First, the samples were preheated in a furnace and passed through the spray booth. As the sample crosses the spray booth, glass was sprayed automatically by the spray gun. After this, the samples were passed to the main oven to fire the glass.

4. Electrical characteristics

4.1. Test

Eight varistor blocks were used for electrical characterization in each case. The varistors were characterized at low, medium and high current. The low current characteristics (mAs) of a varistor block are associated with leakage currents. The medium current range is in the working range of the blocks, usually from a few hundred amperes up to 5 kA or 10 kA depending on the block type. The high current properties of the block will give a measure of their power withstand capability. The leakage currents were measured using a watt loss tester. The high current region was characterized using the high amplitude short duration tester (HA-SD test). For the 42 mm blocks, the peak current amplitude was 100 kA. This region represents the power-limiting condition for protection from high-current spikes such as those generated by lightning strikes.

In the watt loss tester, one sample was placed each time in the measuring chamber and electrical pulses with peak currents of 100 μA, 500 μA, 1 mA and 5 mA were given to the sample at room temperature and the corresponding peak voltage was recorded from the

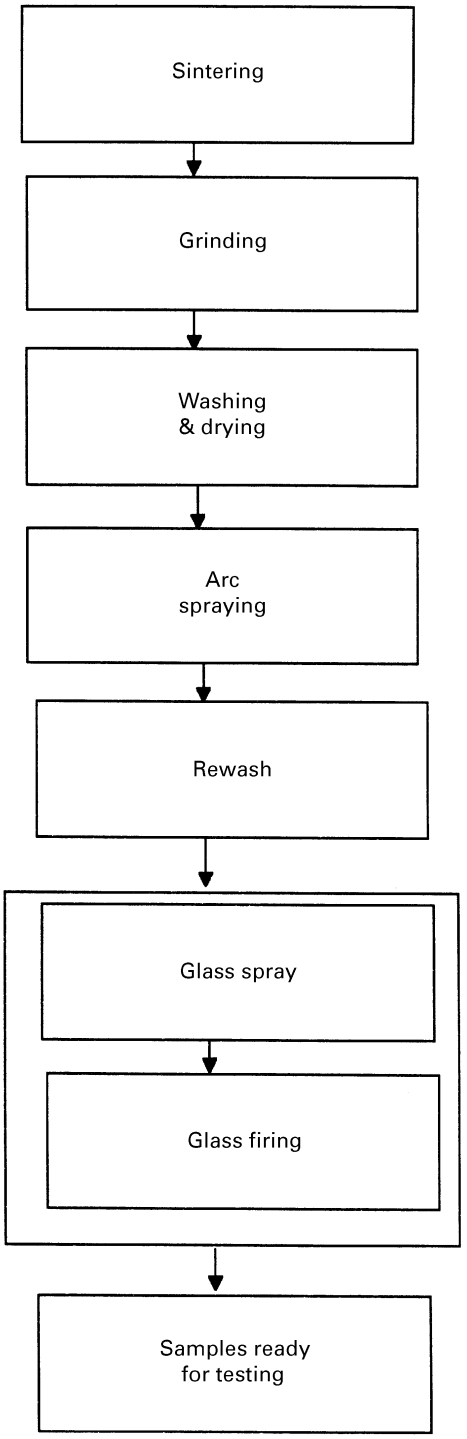

Figure 5 Flow chart of the different processing steps to prepare the varistor samples.

display. The watt loss was also measured at a peak voltage for currents 100 and 500 μA and 80% of peak voltage at 5 mA.

For the 100 A and 10 kA tests, the samples were placed in a fixture at the base of the classifier. The charging voltage was maintained at 29.9 kV and the charging time 5 s. However, the set-up was different for the 100 A and 10 kA test. The results for 100 A were recorded from the display and voltage for 10 kA was marked automatically on the sample after correcting this voltage for an exact current of 10 kA. The 100 kA test is very critical, because at this test an electrical charge with very high frequency is passed through the disc for a very short period as to simulate the test with an actual lightning strike which have very high frequency components, and its duration is of order of 4 μs. Two shots were given simultaneously with 8/20 μs pulse to the samples where 8 μs is needed for the peak and 20 μs is the decay time for 50% of the peak pulse. The shape of the test waves varies with the nature of application. For power apparatus 1.2/50 μs and 8/20 μs wave-shapes are used, whereas for communications applications a 10/560 μs wave-shape is used [3]. Normally the short duration pulse is more detrimental than the long one and cracks of the samples are observed both longitudinally and cross-wise.

4.2. Results and discussion

Table III shows residual voltages at different currents with different firing profiles. It includes, low current region, breakdown region and upturn region. In low current region (100–500 μA), for profile number 1, the steady voltage is lower than that of the other profiles. The no linearity characteristics is defined for currents at 1 and 5 mA. The 100 A test is carried out to see the nature of the I–V curves. The residual voltage at 10 kA is called IR value. Voltage ratio at 10 kA and 5 mA will define if the product is better or not! Though firing profile number 1 has improved the low current characteristics, the IR value is lower than that obtained by the conventional profile. It may be that for the RCS profile, the area between the peak temperature and the 1000 °C temperature is lower than that of the conventional one. As peak temperature is the same in all cases, the IR value depends on the area between the peak temperature and 1000 °C temperature. The upturn region is drawn with the value of voltage for current 100 kA. This test at 100 kA also shows the performance of power withstand capability of the disc.

TABLE III Voltage (kV) at different currents for each profile

Profile number	100 μA	500 μA	1 mA	5 mA	100 A	10 kA	100 kA
1	1.26	6.39	8.8	9.3	11.59	16.48	28.07
2	1.41	6.62	7.89	8.72	11.19	15.93	27.55
3	1.5	6.94	8.15	8.9	11.44	16.2	27.87
4	1.43	6.92	8.61	9.28	11.72	16.55	28.43
5	1.29	6.29	8.07	8.8	11.16	16.05	27.46
6	1.36	6.62	9.09	9.6	11.95	17.18	29.2

The watt loss is associated with pre-breakdown low current region. A comparative study of watt loss is presented in Table IV. Normally the power loss data was taken at 80% of peak voltage at 5 mA. The other two watt loss values at 100 and 500 μA are given for comparison. In all cases, it is seen that profile number 1 shows the lower watt loss, indicating better performance at pre-breakdown region. Watt loss at 100 μA does not vary much with different profiles but at 500 μA and at 80% peak voltage of 5 mA value, watt loss changes as the profile changes.

The most desirable device should have a high value of non-linear coefficient, a low value of leakage current, a long stability life and a high energy absorption capability. Table V shows the values of non-linear coefficient, nominal voltage, leakage current, life stability and energy absorption capability and clamp ratio. The non-linear coefficient was calculated by

$$\alpha = \frac{\log I_2 - \log I_1}{\log V_2 - \log V_1}$$

where I_2 and I_1 are 5 and 1 mA, respectively, and V_2 and V_1 are the residual voltages at I_2 and I_1, respectively. Clamp ratio is defined as the ratio of residual voltage values at 10 kA and 5 mA. Non-linear coefficient varies as the profile changes; profile 1 together with profile 6 shows the highest non-linear coefficient, but energy absorption capability of the product fired with profile 6 shows the lowest value. The product with high non-linear coefficient should not have the highest energy absorption capability. Nominal voltage, leakage current and clamp ratio do not vary much with changes of profile. The I–V characteristics of the samples fired with the above profiles are shown in Fig. 6.

TABLE IV Watt loss (P_d) at 100, 500 μA and 80% voltage of 5 mA

Profile number	P_d at 100 μA	P_d at 500 μA	P_d at 80% peak voltage at 5 mA
1	0.012	0.1408	1.7058
2	0.0119	0.3273	1.7179
3	0.0116	0.3206	1.7528
4	0.012	0.2146	1.7327
5	0.015	0.1726	1.71
6	0.0153	0.18	1.75

5. Microstructural analysis

5.1. Sample preparation

The surface of the sintered specimen was lapped and polished to a mirror-like finish on a micro-cloth polishing wheel using fine SiC paper followed by a final polishing with diamond paste (2, 1 and 0.25 μm particle size). The microstructure of the samples sintered

TABLE V Values of non-linear coefficient, nominal voltage, leakage current, life stability and energy absorption capability for different firing profiles

Profile Number	Non-linear coefficient	Nominal voltage $C = V$ at 1 mA	Leakage current I_R	Life $P_G < P_D$	Clamp ratio	Energy absorption (Initial failure) (J/cm^{-3})
1	29.12	8.8	0.02	Pass	1.77	267
2	16.09	7.89	0.05	Pass	1.82	149
3	18.28	8.15	0.05	Pass	1.81	232
4	21.47	8.61	0.03	Pass	1.78	200
5	18.58	8.07	0.03	Pass	1.82	197
6	29.48	9.09	0.03	Pass	1.78	122

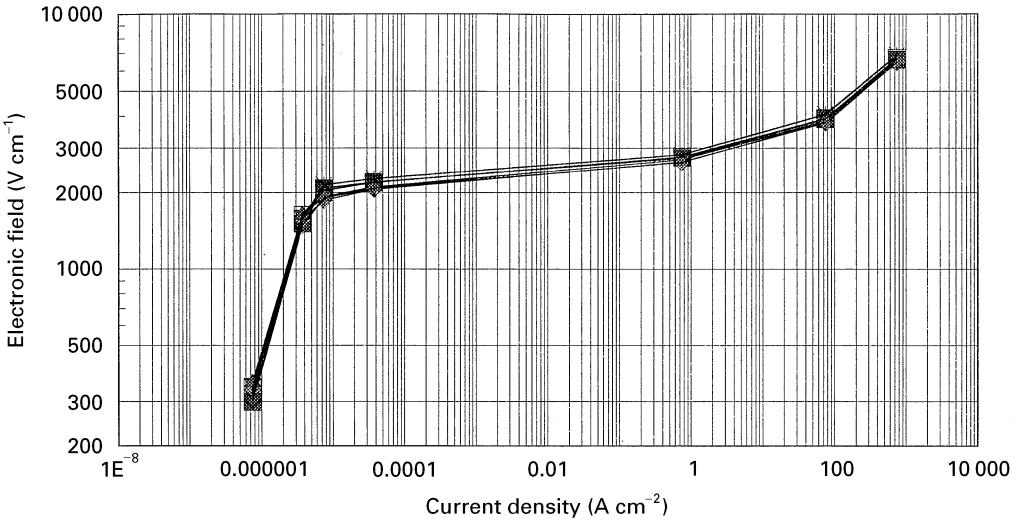

Figure 6 I–V curves of the discs fired with profiles 1(▩), 2(◈), 3(✱), 4(□), 5 (◇) and 6(∗).

with profiles 1, 2, 3, 4, 5 and 6 were observed with a scanning electron microscope (SEM) manufactured by Jeol Ltd. model 840 A at 20 kV. The backscattered electron images (BEI) were taken by SEM. These images of samples sintered with profiles 1, 2, 3, 4, 5 and 6 are shown in Figs 7–12, respectively.

5.2. Discussion

Four basic phases can be observed: wurtzite ZnO, spinel, pyrochlore and several bismuth-rich glassy phases. The location of spinel and pyrochlore is the intergranular phase between the ZnO grains. Bi-rich phases exist mainly at the triple point and pore is exhibited as a black portion. In Fig. 7, it can be seen that the grain size range is between 5–20 μm (average 10 μm). Intergranular porosity is evenly distributed with very small content. The pore size is approximately 1–8 μm. Twinning is evident. Antimony spinel phases and glassy bismuth phases are visible with good distribution between the zinc oxide grains. In Fig. 7, **a** indicates the ZnO phase and pore is shown by **b**. The grain size range for Fig. 8 is 3–20 μm (average 10 μm). The porosity content is low and intergranular. The pore size is approximately 1–4 μm. Twinning is

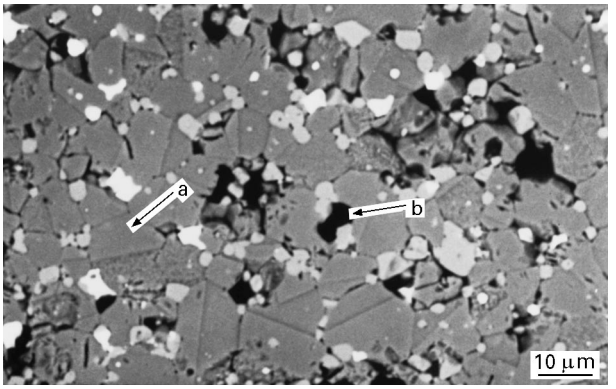

Figure 7 SEM photograph of the disc fired by weight loss rate and shrinkage rate limit 0.75 g kg^{-1} h^{-1} and 10 μm mm^{-1} h^{-1}, respectively. a, ZnOphase; b, pore.

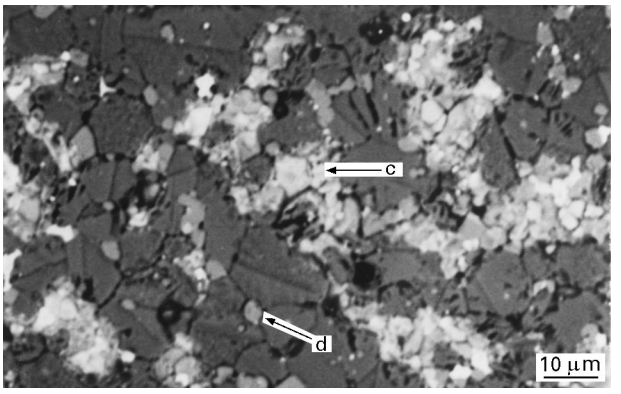

Figure 8 SEM photograph of the disc fired by weight loss rate and shrinkage rate limit 3 g kg^{-1} h^{-1} and 10 μm mm^{-1} h^{-1}, respectively. c, spinel; d, bismuth-rich phases.

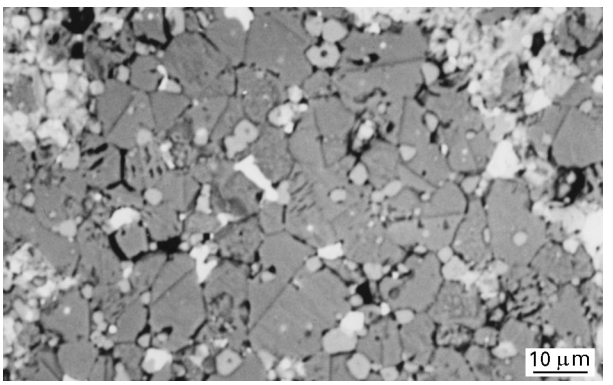

Figure 9 SEM photograph of the disc fired by weight loss rate and shrinkage rate limit 0.75 g kg^{-1} h^{-1} and 40 μm mm^{-1} h^{-1}, respectively.

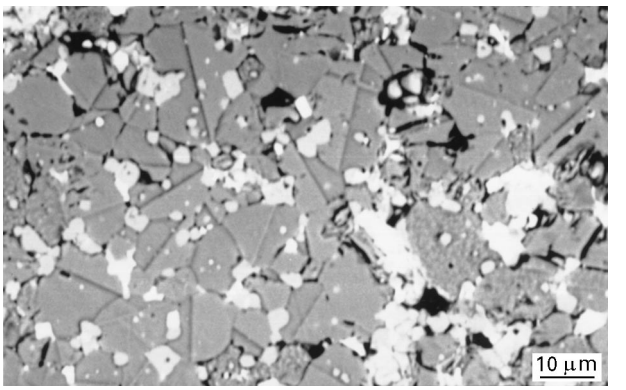

Figure 10 SEM photograph of the disc fired by weight loss rate and shrinkage rate limit 3 g kg^{-1} h^{-1} and 40 μm mm^{-1} h^{-1}, respectively.

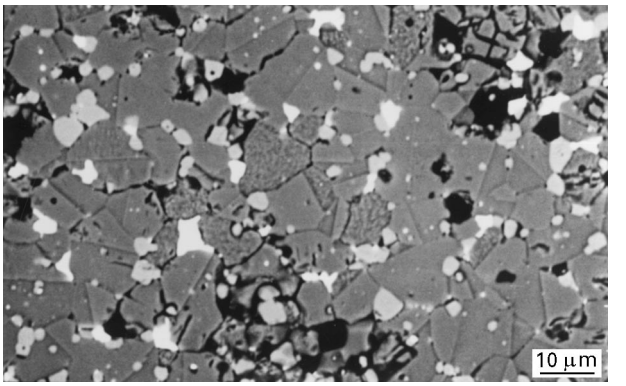

Figure 11 SEM photograph of the disc fired by weight loss rate and shrinkage rate limit 1.5 g kg^{-1} h^{-1} and 20 μm mm^{-1} h^{-1}, respectively.

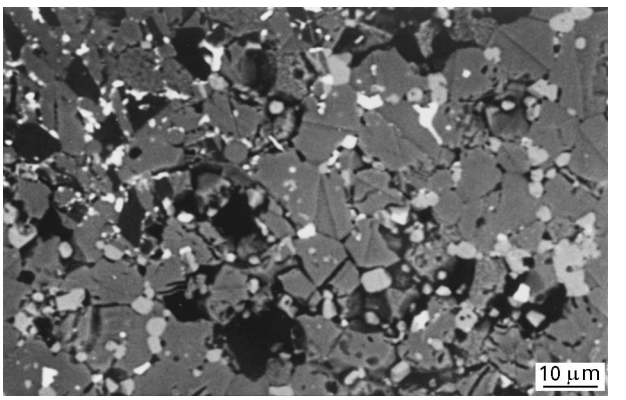

Figure 12 SEM of the discs fired by the classic profile.

evident in some grains. Antimony spinel phase and glassy bismuth phase are visible; however these phases are not evenly distributed between the zinc oxide grains, and can be seen that they are clumped together. The spinel- and bismuth-rich phases are shown by **c** and **d**, respectively. In Fig. 9, it is seen that the grain size range is 3–20 μm (average 10 μm). Porosity content is low and primarily intergranular. Pore size is approximately 1–4 μm. Twinning is evident in some grains. Antimony spinel phase and glassy bismuth phase are visible. However, in some areas these phases are not evenly distributed between the zinc oxide grains and can be seen that they are clumped together.

The grain size range in Fig. 10 is 5–20 μm (average 12 μm). Porosity content is low and primarily intergranular. Pore size is approximately 1–10 μm. Twinning is evident in some grains. Antimony spinel phase and glassy bismuth phase are visible. These phases are reasonably well distributed between the zinc oxide grains. Grain size range in Fig. 11 is 5–15 μm (average 8 μm). Porosity is primarily intergranular with some intragranular. Pore size is approximately 1–5 μm. Twinning is evident in some grains. Antimony spinel phase and glassy bismuth phase are also visible. These phases are reasonably well distributed between the zinc oxide grains. It is seen in Fig. 12 that the grain size range is 5–25 μm (average 10 μm). It is very porous. Porosity is primarily intergranular with some intragranular. Pore size is approximately 1–20 μm. Twinning is again evident in some grains. Antimony spinel phase and glassy bismuth phase are visible. These phases are reasonably well distributed between the zinc oxide grains.

Twinning can be seen in both types of samples fired with RCS and conventional profiles. Twinning occurs naturally, and no effect in the electrical property of the product has been identified. The phases for profile 1 are more uniformly distributed than that of for profiles 2 and 3, as shown in Figs 7, 8 and 9. These properly distributed phases improve the pre-breakdown characteristics, as shown in Table III, which is in agreement with reference [2]. Porosity distribution and size are the main factors for the energy absorption capability. As shown in Fig. 12, it is seen that the product fired with conventional profile is porous and has the lowest energy absorption capability, as seen in Table IV. This is in agreement with reference [7]. It is detrimental for the product if porosity and different phases are intragranular. Figs 7, 8 and 9 for samples fired with RCS profiles show that all pores are intergranular.

6. Conclusions

1. The distribution of different phases in the microstructure can changed by using rate-controlled sintering, which affects the pre-breakdown region of the varistor.
2. The porosity level and its distribution size can be modified by rate-controlled sintering.
3. The non-linear coefficient and power loss can be improved by rate-controlled sintering.
4. Energy absorption capability can also be improved by using rate-controlled sintering.

Acknowledgements

This study has been carried out as part of DOCERPO project with Brite/Euram II programme (Contract No. BRE2.CT92.0148) and the authors gratefully acknowledge the financial support provided by the Commission of the European Communities.

References

1. M. MATSOUKA, *Jpn. J. Appl. Phys.* **10** (1971) 736.
2. T. K. GUPTA, *J. Amer. Ceram. Soc.* **73** (7) (1990) 1840.
3. Transient Voltage Suppression Devices, Publication, Harris Semiconductor, 1994.
4. R. EINZIGER, *Ann. Rev. Mater. Sci.* **17** (1987) 299.
5. E. OLSSON, L. K. L. FALK and G. L. DUNLOP, *J. Mater. Sci.* **20** (1985) 4091.
6. T. ASOKAN, G. N. K. IYENGAR and G. R. NAGABHUSHANA, *ibid.* **22** (1987) 2229.
7. T. O. SOKOLY, M. A. SEITZ, J. P. GUERTIN, P. P. SCHUMACHER and M. E. POTTER, EPRI, EL-1647, Project 425-1, Final report, December 1980.
8. L. M. LEVINSON and H. R. PHILIPP, *Ceram. Bull.* **64** (4) (1986) 639.
9. T. K. GUPTA, in "Tailoring multiphase and composite ceramics", edited by R. E. Tressler, G. L. Messing, C. G. Pantino and R. E. Newnham (Plenum, New York, 1986) p. 493.
10. W. G. CARLSON and T. K. GUPTA, *J. Appl. Phys.* **53** (1982) 5746.
11. T. MIYOSHI, K. MAEDA, K. TAKAHASHI and T. YAMAZAKI, in: "Advances in ceramics", Vol. 1, edited by L. M. Levinson and D. Hill (American Ceramic Society, Columbus, OH, 1981) p. 309.
12. T. TAKEMURA and M. KOBAYASHI, in: "Advances in ceramics", Vol. 1, edited by L. M. Levinson and D. Hill (American Ceramic Society, Columbus, OH, 1981) p. 50.

Received 23 June 1995
and accepted 17 June 1997